Available online at www.sciencedirect.com

SCIENCE DIRECT®

Nuclear Medicine and Biology 33 (2006) 217–226

NUCLEAR MEDICINE — AND — BIOLOGY

www.elsevier.com/locate/nucmedbio

Three-dimensional maximum a posteriori (MAP) imaging with radiopharmaceuticals labeled with three Cu radionuclides

Ananya Ruangma[a,1], Bing Bai[b], Jason S. Lewis[a], Xiankai Sun[a], Michael J. Welch[a], Richard Leahy[b], Richard Laforest[a,*]

[a]*Mallinckrodt Institute of Radiology, Washington University School of Medicine, St. Louis, MO 63110, USA*
[b]*Signal and Image Processing Institute, University of Southern California, Los Angeles, CA 90089, USA*

Received 16 August 2005; received in revised form 17 October 2005; accepted 8 November 2005

Abstract

Background: One of the limiting factors in achieving the best spatial resolution in positron emission tomography (PET), especially in small-animal PET, is the positron range associated with the decay of nuclides, and usual PET image reconstruction algorithms do not provide a correction for the positron range. This work presents initial results obtained with the maximum a posteriori (MAP) algorithm, which has been developed to include an accurate model of the camera response, the Poisson distribution of coincidence data and the fundamental physics of positron decay including the positron range.

Methods: Phantoms were imaged with three positron emitting isotopes of Cu (^{60}Cu, ^{61}Cu and ^{64}Cu), and mice and rats were imaged with two radiopharmaceuticals labeled with these isotopes in a microPET-R4 camera. These isotopes decay by positron emission with very different end-point energies resulting in wildly different spatial resolutions. Spatial resolution improvement and image quality offered by the MAP algorithm were studied with the line source phantom and a miniature Derenzo phantom. In addition, three mice and three rats were sequentially injected over a 48-h period with Cu-pyruvaldehyde bis(N^4-methylthiosemicarbazone) (for blood flow to organs) and Cu-1,4,7,10-tetraazacyclododecane-1,4,7-tri(methanephosphonic acid) (for bone imaging) labeled with the said three isotopes of Cu.

Results: The line source experiment showed that comparable spatial resolution is possible with all three isotopes when using the positron range correction in MAP. The in vivo images obtained from ^{60}Cu and ^{61}Cu and reconstructed with 2D filtered back projection algorithms provided by the camera manufacturer show reduced clarity due to degraded spatial resolution arising from the extended positron ranges as compared with ^{64}Cu. MAP reconstructions exhibited a higher resolution with clearer organ delineation.

Conclusion: Inclusion of a positron range model in the MAP reconstruction algorithm may potentially result in significant resolution recovery for isotopes with larger positron ranges.

Keywords: MAP; PET; Positron range; Cu radionuclides

1. Introduction

A wide range of biologic processes can be studied using positron emitting nuclides attached to biologic compounds and positron emission tomography (PET). A great advantage of this technique is its ability to provide quantitative measurement of a radiotracer in vivo. Quantitative PET has been established for a few standard radionuclides such as ^{18}F, ^{11}C, ^{13}N and ^{15}O; in addition, with the advent of novel nonstandard positron-emitting nuclides, new radiopharmaceuticals can be labeled, new biologic pathways can be imaged and quantitative measurement of activity concentration can be performed noninvasively and repeatedly. High-resolution PET cameras have been developed for the imaging of small animals, and this technology is increasingly used in drug discovery and development [1]. However, many of the novel nuclides decay with the emission of high-energy positrons that travel for a long distance in tissues before annihilating and thus produce

* Corresponding author. Tel.: +1 314 362 8423; fax: +1 314 362 5428.
E-mail addresses: ruangmaa@wustl.edu (A. Ruangma), laforestr@wustl.edu (R. Laforest).
[1] Washington University School of Medicine, Campus Box 8225, 510 South Kingshighway Boulevard, St. Louis, MO 63110, USA. Tel.: +1 314 362 8423; fax: +1 314 362 5428.

0969-8051/$ – see front matter © 2006 Elsevier Inc. All rights reserved.
doi:10.1016/j.nucmedbio.2005.11.001

Table 1
Cu radionuclide decay properties

Radionuclide	Half-life	Percentage positron decay (%)	Maximum β energy (MeV)	Average positron range (mm)
^{60}Cu	23.7 min	92.5	3.772	3.09
^{61}Cu	3.333 h	61.5	1.215	1.32
^{64}Cu	12.7 h	17.4	0.653	0.57

The average positron ranges were calculated from EGS4 simulation in soft tissue.

images with degraded spatial resolution. In particular, high-resolution PET images will be greatly degraded and a positron range correction is necessary to improve resolution and contrast when imaging with such isotopes is performed.

Over the past several years, PET has undergone a very rapid development due to reasons such as technological development, the multitude of new tracer substances available, the clinical acceptance of the imaging modality and the Medicare reimbursement of FDG-PET for human use. However, only a few radiopharmaceuticals labeled with nonstandard nuclides have been investigated in humans. At the Washington University School of Medicine, nonstandard PET isotopes such as ^{76}Br, ^{77}Br, ^{124}I, ^{86}Y, ^{94m}Tc, ^{66}Ga, ^{60}Cu, ^{61}Cu and ^{64}Cu are currently produced for biomedical research [2–4]. These isotopes possess half-lives of an hour to a few days, allowing for the study of radiopharmaceutical kinetics over a period of up to a few days. However, these nonstandard positron emitters are generally characterized by high-positron end-point energy and emission of numerous nonannihilation gamma rays, both of which contribute to the degradation of PET images.

Recently, an image reconstruction algorithm—a maximum a posteriori (MAP) reconstruction algorithm [5]—that includes an accurate model of the camera response, the Poisson distribution of coincidence data and corrections for photon noncollinearity has been developed. This reconstruction algorithm was initially developed for the CTI/Siemens ECAT 962 scanner [6,7] and UCLA microPET [8] and was followed by a recent adaptation to the CTI-Concorde MicroSystems animal scanners. In particular, this algorithm has been shown to improve spatial resolution and, at the same time, maintain the noise level. In Reference [8], it was demonstrated that noise was reduced with this technique at a comparable spatial resolution. MAP image reconstruction is a Bayesian reconstruction method used in the reconstruction of PET images [5]. The method combines an accurate physical model of photon-pair detection with a Poisson statistical model of the random nature of the detected events. These models are incorporated in a likelihood function and combined through Bayes theorem with a prior distribution or smoothing function that reflects the expectation that reconstructed images will be locally smooth. Maximizing the resulting posterior probability distribution results in the MAP image. We report on an extension of this algorithm that includes a model of the positron range in the projection model and hence attempts to correct the reconstructed images for resolution loss due to positron range [9].

^{60}Cu, ^{61}Cu and ^{64}Cu are nonstandard positron-emitting radionuclides that are being produced on demand at the Washington University School of Medicine [2,3]. Their decay properties are summarized in Table 1. ^{64}Cu also decays by β^- (39%), which makes it an attractive isotope for dual use of imaging and therapy [10–17]. The positron range of ^{64}Cu is approximately the same as that of ^{18}F; as such, the spatial resolution is only weakly increased in microPET imaging due to the positron range for this isotope. The large positron maximum energy results in long positron ranges, particularly up to a few centimeters for ^{60}Cu in tissue. Such an extended positron range has a minimal impact on spatial resolution in clinical PET imaging [18] but is very detrimental in small-animal PET where a resolution <1 mm is sought. To illustrate the possible usefulness of the MAP reconstruction algorithm for correction of positron range, we performed imaging experiments with phantom and line sources as well as animal experiments with the abovementioned isotopes of Cu. In the in vivo studies, animals were injected with agents labeled with each of the three PET isotopes of Cu. The radiopharmaceuticals were chosen carefully; Cu-pyruvaldehyde bis(N^4-methylthiosemicarbazone) (Cu-PTSM) is a blood-flow agent [14,16,17] that shows uptake in all major organs whereas Cu-1,4,7,10-tetraazacyclododecane-1,4,7-tri(methanephosphonic acid) (Cu-DO3P) is a bone-seeking agent [19] that produces images of the skeleton and thus provides a measure of the spatial resolution improvement in animal data.

2. Materials and methods

2.1. Radionuclide and radiopharmaceutical production

The three radionuclides, ^{60}Cu, ^{61}Cu and ^{64}Cu, were produced on the CS-15 biomedical cyclotron at the Washington University School of Medicine using published methods [2,3]. These isotopes are all produced by a (p,n) reaction on the appropriate enriched Ni target material electrodeposited onto a Au target. Separation and purification of irradiated Ni material from the Cu radionuclide proceed by ion exchange chromatography. All three radionuclides are produced with high radiochemical purity and high specific activity. Two radiopharmaceuticals were used for the animal studies, Cu-PTSM [16,20] and Cu-DO3P [19]. ^{64}Cu-, ^{61}Cu- and ^{60}Cu-PTSM were produced based on methods reported in the literature [20,21]. Briefly, the radiocomplexes were produced by the addition of H_2(ATSM) (in DMSO) to the chloride form of the desired radionuclide ($CuCl_2$). After a few minutes, the complexes were purified by using C_{18}-SepPak Light solid-phase extraction cartridges. The radiochemical purity (>98%) was determined by radioTLC. ^{64}Cu-, ^{61}Cu- and ^{60}Cu-DO3P were also produced according to literature methods [19]. $^{64}CuCl_2$ was converted to ^{64}Cu-acetate by

stirring with 0.4 M of ammonium acetate (pH 6.5). This was then added to the DO3P ligand solution (2.0–5.0 mM) and allowed to react for 2 h at room temperature. The radiochemical purity was determined by reversed-phase TLC. Unless otherwise stated, all chemicals were purchased from Sigma-Aldrich Chemical (Milwaukee, WI, USA). All solutions were prepared using distilled deionized water (Milli-Q; >18 MΩ resistivity).

2.2. Imaging system

Small-animal PET imaging was conducted on a microPET-R4 scanner (CTI-Concorde MicroSystems, Knoxville, TN, USA), for which system performance and characterization have been reported in Reference [22]. The microPET-R4 consists of 24 detectors arranged in four contiguous rings with a ring diameter of 14.8 cm and an axial extent of 8 cm. Each detector consists of a single block of lutetium oxyorthosilicate (LSO) crystal subdivided into an 8×8 array coupled to a position-sensitive photomultiplier tube with a bundle of coherent fiber optic. Each LSO crystal measures $2\times2\times10$ mm^3 and is assembled on a 2.4-mm pitch. The space between each crystal is filled with TiO_2 powder to ensure scintillation light reflection. The system is capable of a <2.0-mm resolution at the center of the field of view (CFOV) when imaging is performed with a short-range positron emitter such as ^{18}F. Typical resolution is of the order of 2.3 mm and the absolute sensitivity of the camera is 3.4% for a point source placed at the CFOV.

2.3. Reconstruction algorithms

At the core of the MAP approach is the model for detected events or sinogram data, **y**, whose expected value can be expressed in matrix–vector form as shown in Reference [5]:

$$\mathbf{y} = \mathbf{P}\mathbf{x} + \mathbf{r} + \mathbf{s} \quad (1)$$

where **x** is the estimated image, **r** is the mean of the randoms and **s** is the mean of the scattered events. **P** is the system matrix describing the probability that an unscattered event is detected, which is factored as follows:

$$\mathbf{P} = \mathbf{P}_{\text{norm}}\mathbf{P}_{\text{blur}}\mathbf{P}_{\text{attn}}\mathbf{P}_{\text{geom}}\mathbf{P}_{\text{range}} \quad (2)$$

where $\mathbf{P}_{\text{norm}}$ is a diagonal matrix containing the normalization factors for unscattered events; $\mathbf{P}_{\text{blur}}$ is a blurring operator that models photon-pair noncollinearity, intercrystal scatter and crystal penetration; $\mathbf{P}_{\text{attn}}$ is a matrix containing the attenuation factors for each detector pair; $\mathbf{P}_{\text{geom}}$ is the geometric projection matrix describing the probability that a photon pair reaches the front faces of the detector pair in the absence of attenuation and assuming perfect photon-pair collinearity; and $\mathbf{P}_{\text{range}}$ models the positron range effect as described subsequently. Randoms are handled in the standard manner through subtraction of a set of delayed coincidence events. This subtraction of counts affects the statistical distribution of the data that we account for using the shifted Poisson model [6,23].

In MAP reconstruction, a hyperparameter β is used to control the smoothness of the image. One of the advantages of using MAP as compared with other maximum likelihood-based methods (e.g., OSEM) is that we can choose the value of this hyperparameter to achieve optimal tradeoff between image resolution and noise.

The positron range kernels were calculated from a calculation of the positron ranges of ^{60}Cu, ^{61}Cu and ^{64}Cu with EGS4+PRESTA (Electron Gamma Shower Code Version 4+ Parameter Reduced Electron Step Transport Algorithm), which simulates the propagation of electrons, positrons and high-energy photons in matter [24–26]. A point source of a given isotope in which the initial energy of the particles was distributed along Fermi functions was simulated. In these calculations, the complete decay scheme was included as described in Reference [4]. In short, for each transition leading to an excited state in the daughter nuclei, the positron kinetic energy spectra were modeled with a FERMI function with end point given by the Q value to this excited level. The combined energy spectrum was then obtained by summing all transitions with their corresponding branching ratio. The average positron ranges from these simulations are reported in Table 1.

In addition to the MAP reconstruction, images were also reconstructed with standard Fourier rebinning (FORE) 2D filtered back projection (FBP) algorithms provided by the camera manufacturer. The initial 3D sinograms were rebinned using (FORE) before applying 2D FBP. This algorithm does not model the process of gamma detection or the physics of positron decay. A ramp filter with frequency cutoff set at the Nyquist frequency was used. The prompt gammas from ^{60}Cu and ^{61}Cu data were eliminated by first subtracting a uniform background in the sinograms caused by the coincidence of annihilation photons with cascade gamma rays before image reconstruction. This procedure is similar to scatter correction and does not affect the spatial resolution in the images.

2.4. Phantom studies

Degradation of spatial resolution due to positron range was studied using a line source phantom and a miniature Derenzo phantom. The line source experiments were performed using thin plastic tubing with an inner diameter of 0.5 mm inserted in a water-filled chamber (25.4 mm in diameter and 25.4 mm in length). For each study, a concentrated ^{60}Cu, ^{61}Cu or ^{64}Cu solution was injected into the small plastic tube and the phantom was aligned at the CFOV. The phantom was then imaged for a single frame for 30 min. The energy acceptance window was set to 250–750 keV with a 10-ns timing window. A value of the hyperparameter β of .01 was chosen for these reconstructions. Although reconstruction was performed with several values of the hyperparameter, this value was finally chosen as it provided the best spatial resolution.

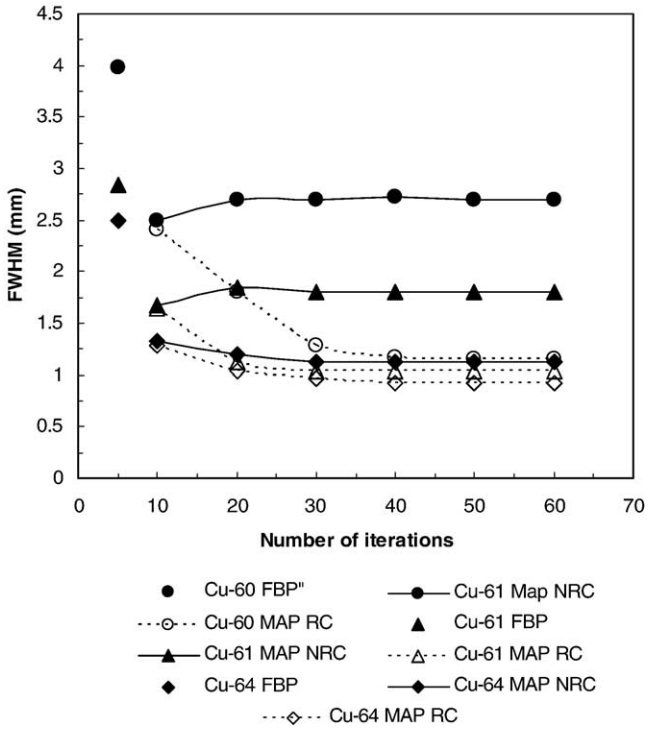

Fig. 1. Line-spread-function measurement from a line source phantom for images reconstructed from 2D FBP, MAP and MAP+RC for ^{60}Cu, ^{61}Cu and ^{64}Cu.

The miniature Derenzo phantom was constructed within our laboratories and was based on the original design of Derenzo et al. [27], but with smaller rod sizes and rod–rod separation distance. This phantom was imaged with all three isotopes separately. The phantom has an inner diameter of 60 mm and contains fillable hot rods of different diameters (1.0, 1.25, 1.5, 2.0 and 2.5 mm) separated by four times their diameter arranged in five segments. The length of the rods is 38 mm. The phantom was filled with the ^{60}Cu, ^{61}Cu or ^{64}Cu solution and scanned for one frame of 30 min for ^{60}Cu and ^{61}Cu and one frame of 60 min for ^{64}Cu. Images were reconstructed with 2D FBP and with MAP (with and without range correction). For MAP reconstructions, the β hyperparameter was set to .001, .01 and .1 and the number of iterations varied from 10 to 50, respectively.

2.5. Animal studies

All animal experiments were conducted in compliance with the Guidelines for the Care and Use of Research Animals established by the Washington University Animal Studies Committee. All imaging studies were performed in a temperature-controlled imaging suite with close monitoring of the physiological status of the animals. To eliminate fluctuations due to physiological differences among animals, we used the same animals to study the same compounds labeled with the three Cu isotopes over a 48-h period. In all cases, the animals were scanned at 10 min postinjection for Cu-PTSM and 35 min postinjection for Cu-DO3P for a single frame of 5 min. The animals were first injected with the ^{60}Cu-labeled compounds and scanned on microPET-R4. Four hours were allowed for the complete decay of ^{60}Cu, and then imaging of the same animals was performed with the ^{61}Cu analogs. On the following day (allowing for ^{61}Cu decay), the same animals were injected with the ^{64}Cu compounds. The injected activity was designed to provide an equal number of positron decays during the 5-min scan for each isotope. The images were reconstructed with standard reconstruction algorithms available from Concorde Microsystems (2D FBP and 2D OSEM) as well as with MAP with positron range correction (MAP+RC) and without (MAP). The β hyperparameter was set at .01 for the reconstruction of the animal experiments to achieve the best spatial resolution and to be consistent with the phantom experiments. The 2D OSEM implemented by the manufacturer does not include modeling of either the detection of gamma rays or the positron annihilation.

3. Results

3.1. Line spread function

The line source phantom studies were reconstructed with 2D FBP, MAP and MAP+RC. The full width at half maximum (FWHM) of the line source for each image was measured from the line spread function constructed from a profile traced through the pixel of highest intensity. Fig. 1

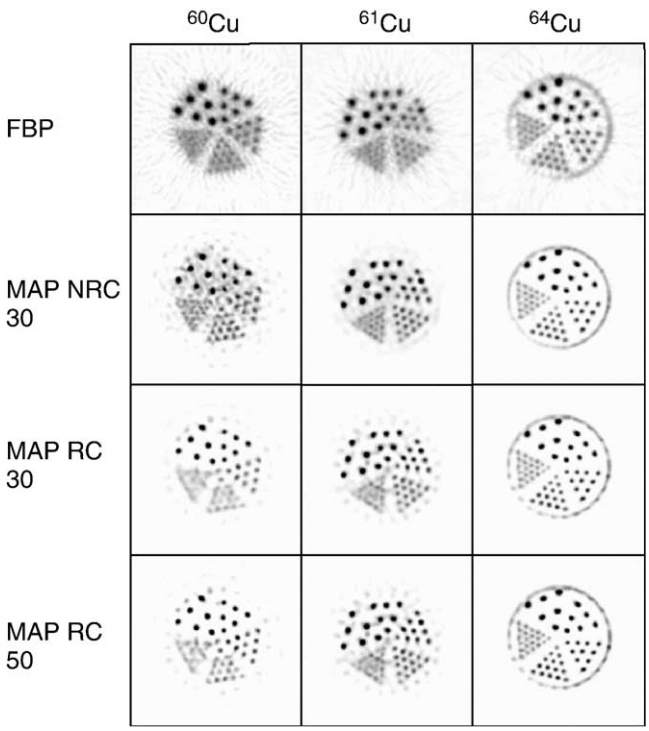

Fig. 2. The miniature Derenzo hot rod phantom images of ^{60}Cu, ^{61}Cu and ^{64}Cu reconstructed with 2D FBP, 2D OSEM, MAP (30 iterations) and MAP+RC (30 and 50 iterations). The rod diameters of the phantom are 1.0, 1.25, 1.5, 2.0 and 2.5 mm.

shows the line-spread-function measurement of the three Cu isotopes. The FWHM on the MAP reconstructions is plotted for various numbers of iterations. The FWHM for the longest-range isotope on the 2D FBP reconstructed images is almost twice that of the shortest (3.7 mm for ^{60}Cu vs. 2.5 mm for ^{64}Cu). The FWHMs of MAP-reconstructed images plateau at 1.1, 1.8 and 2.7 mm for ^{64}Cu, ^{61}Cu and ^{60}Cu, respectively, whereas those of MAP+RC-reconstructed images plateau at 0.9, 1.0 and 1.1 mm, respectively. For the short-range positron isotope, MAP improves the image resolution by a factor of two as compared with 2D OSEM and 2D FBP (FWHM of 1.1 mm vs. 2.0 and 2.5 mm, respectively) and MAP+RC improves it further with an FWHM of 0.9 mm. For the long-range positron ^{60}Cu data, MAP+RC significantly improves the resolution as compared with 2D FBP and MAP (FWHM 1.07 mm vs. 4.0 and 2.6 mm, respectively). Furthermore, the FWHMs from images reconstructed with MAP+RC plateau at 30 iterations, whereas the iteration number does not significantly affect the FWHM for images reconstructed with MAP beyond 15–20 iterations. Also apparent in Fig. 1 is that a longer-range positron emitter requires more iterations to reach the plateau and that the FWHMs of the line sources for each Cu isotope are similar when images are reconstructed with MAP+RC, although each has a unique positron range.

3.2. Image quality

The images of the miniature Derenzo hot rod phantom with ^{60}Cu, ^{61}Cu and ^{64}Cu reconstructed with 2D FBP, MAP and MAP+RC (30 and 50 iterations) are shown in Fig. 2. Only the images reconstructed with the smallest value of the hyperparameter are presented in this figure as it was observed that rod separation was optimal with this value. All the images were reconstructed with scatter correction and attenuation correction applied. The apparent ring around the rod patterns in the ^{64}Cu images is due to residual activity around the rod inserts in the phantom. The 1-mm rods with

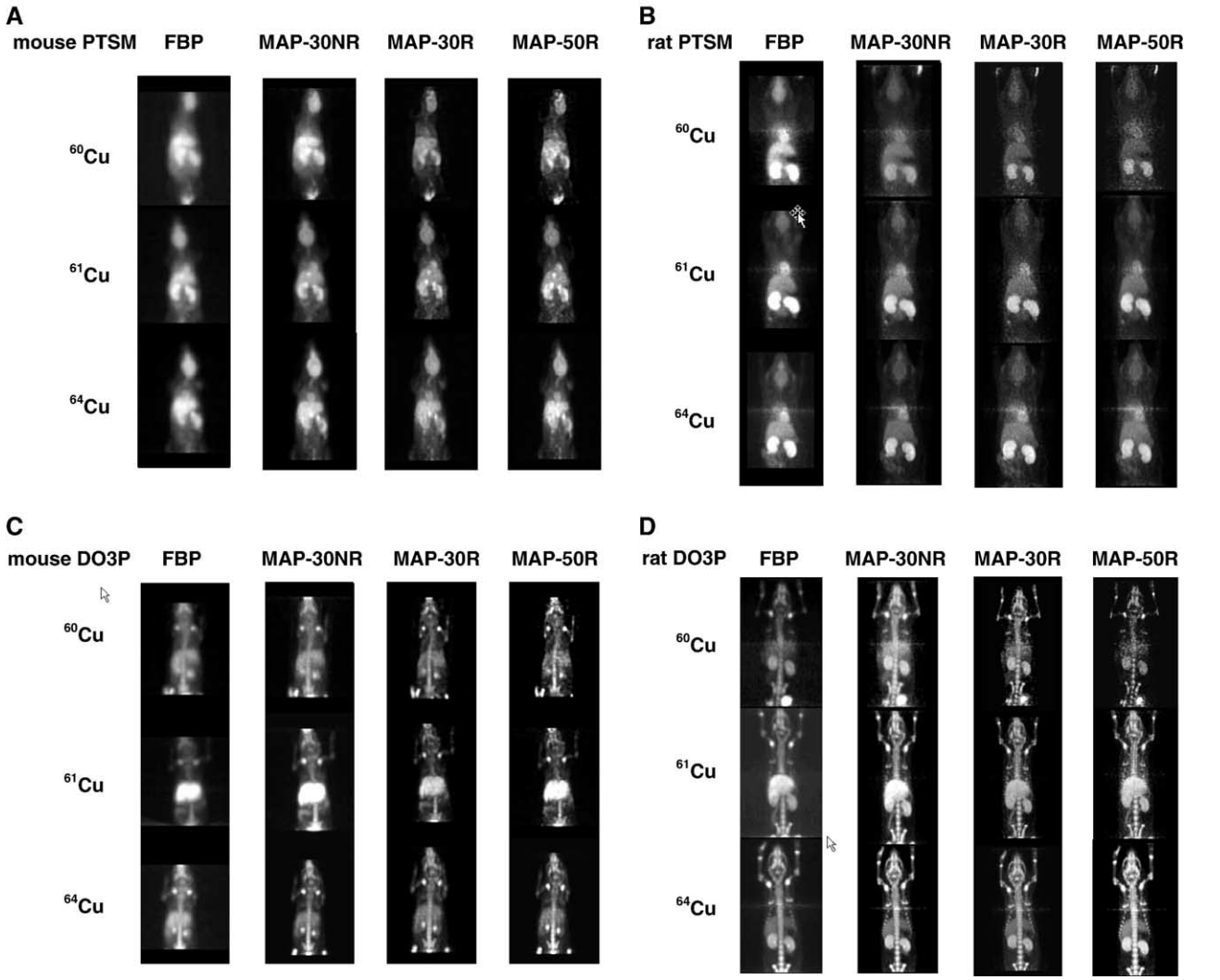

Fig. 3. The maximum intensity projection images reconstructed with OSEM, MAP (30 iterations) and MAP+RC (30 and 50 iterations). (A) A mouse injected with Cu-DO3P labeled with each of the three Cu isotopes. (B) A rat injected with Cu-DO3P. (C) A mouse injected with Cu-PTSM. (D) A rat injected with Cu-PTSM.

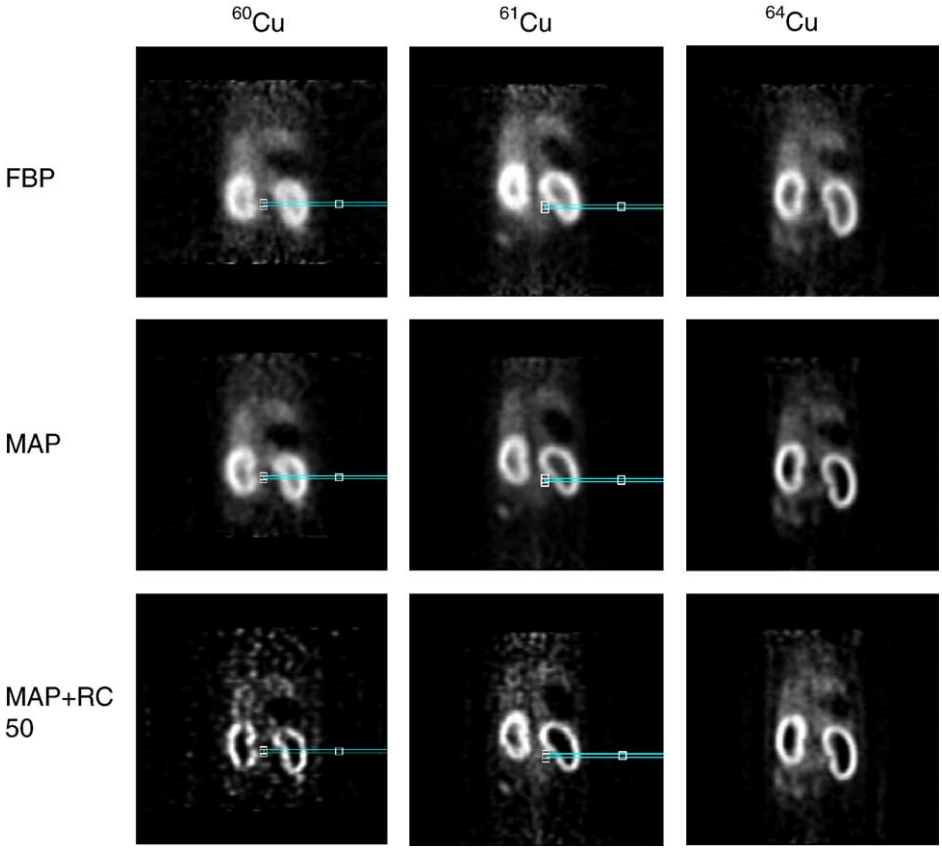

Fig. 4. Coronal slice images of the rat injected with Cu-PTSM. The images were reconstructed with 2D FBP, MAP (30 iterations) and MAP+RC (50 iterations).

^{64}Cu can be barely resolved with FBP and identification of all the rods is possible with MAP, whereas the range correction provides the best rod separation. A similar observation can be made for ^{61}Cu, where it can be seen that 50 iterations yield better rod separation. For ^{60}Cu, the best rod identification is obtained with MAP without range correction for the smallest rods whereas MAP+RC and 50 iterations are better for all the other rod groups. It can also be observed that the rod shape is slightly oblong, especially for ^{64}Cu. This artifact is not due to the range correction in MAP as it is visible for all MAP reconstructions. We can also note a small increase in noise in the images especially at higher numbers of iterations.

Circular artifacts are apparent on the ^{60}Cu and ^{61}Cu images and are due to a mismatch in normalization. The counts seen at the edge of the phantom are caused by the residual activity surrounding the Derenzo insert, highly apparent as a ring in ^{64}Cu images and amplified in MAP+RC images.

3.3. Animal studies

In the animal studies, the data were reconstructed with 2D FBP, 2D OSEM, MAP for 30 iterations and MAP+RC for 30 and 50 iterations. The maximum intensity projection images of a mouse (A) and a rat (B) injected with Cu-DO3P as well as a mouse (C) and a rat (D) injected with Cu-PTSM are shown in Fig. 3. The vertebrae of the mouse and rat injected with Cu-DO3P can be seen with better definition in the images reconstructed with MAP+RC for all Cu isotopes than in images reconstructed with 2D FBP or MAP without range correction. Without the range correction, images using the long-range positron emitter ^{60}Cu are clearly more blurred. In general, the skeletal structure of the animal is more easily identifiable from the surrounding organs in reconstructions with the positron range correction. For Cu-PTSM, generally, MAP reconstruction gives better quality images than 2D FBP recognized by internal organs that are more apparent in the images, especially those reconstructed with MAP+RC. In particular, for ^{61}Cu-PTSM in mice, the kidneys are more delineated from the liver and the gall bladder is more distinct from the liver. The internal organs in the rat data appear more uniform with MAP reconstruction and with better separation than with FBP image reconstruction.

Fig. 4 shows coronal images through the kidneys of the rat injected with Cu-PTSM. The images were reconstructed with 2D FBP, MAP (30 iterations) and MAP+RC (50 iterations). Images of the short-range positron emitter (^{64}Cu) show accumulation of Cu-PTSM mostly in the cortex of the rat kidney, whereas the longer-range emitter images reveal a low amount of tracer localized to the medulla. In particular, FBP images with ^{60}Cu are blurry

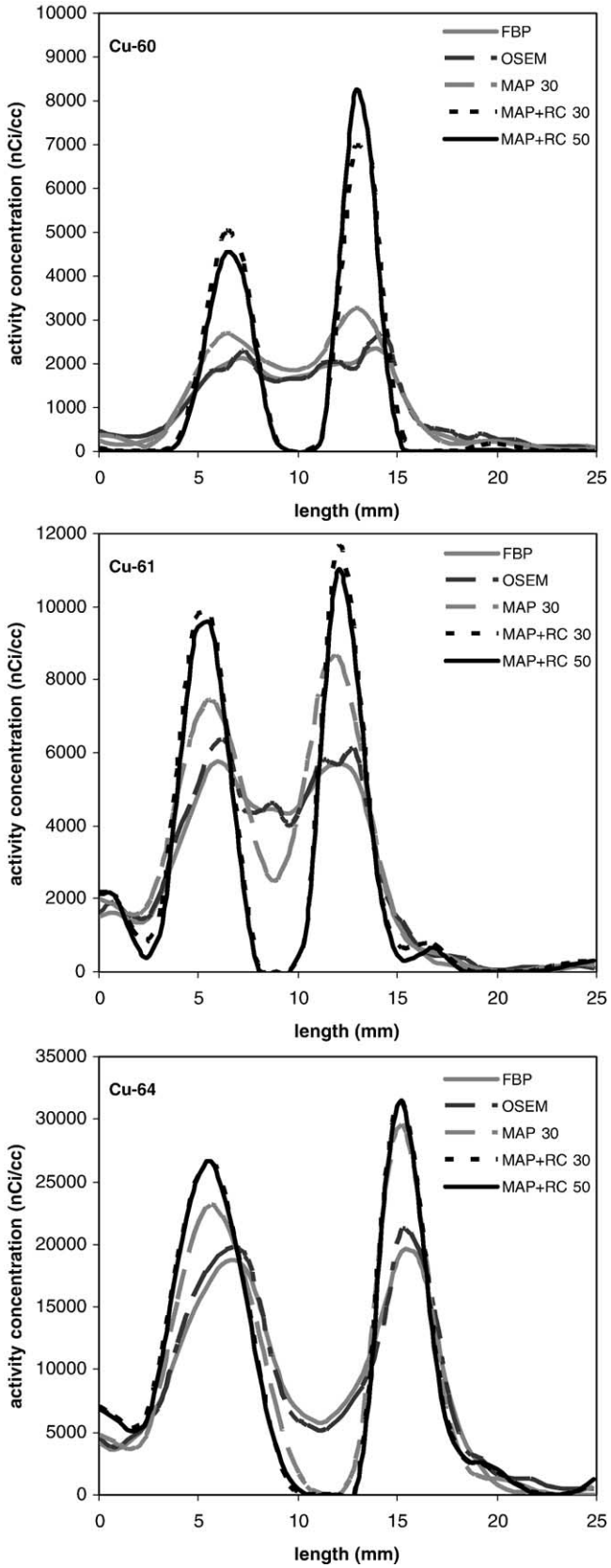

Fig. 5. Line profiles across the kidney of the rat injected with Cu-PTSM from images reconstructed with 2D FBP, 2D OSEM, MAP (30 iterations) and MAP+RC (30 and 50 iterations).

and show considerable accumulation of activity in the medulla of the kidneys. It is also apparent on these images that the noise structure has substantially increased on MAP images especially at 50 iterations. A more detailed inspection can be obtained from line profiles traced across the kidneys, and those allow evaluation of the effect of the positron range correction on this configuration of activity distribution. Those are shown in Fig. 5 for images reconstructed with 2D FBP, 2D OSEM, MAP (30 iterations) and MAP+RC (30 and 50 iterations). Images reconstructed with 2D FBP show higher uptake in the medulla for ^{60}Cu than for ^{64}Cu. Images reconstructed with 2D OSEM show some activities in the medulla, but images reconstructed with MAP show minimal uptake in the same region for all three isotopes. The line profiles from the images reconstructed with MAP+RC show most of the renal activity in the cortex and no medulla activity, even with ^{60}Cu-PTSM. Line profiles from ^{60}Cu, ^{61}Cu and ^{64}Cu are similar when the images are reconstructed with MAP+RC. The peak values representing the uptake in the cortex are almost three times higher for ^{60}Cu when the images were reconstructed with MAP+RC than with 2D OSEM or 2D FBP. For ^{64}Cu, the peak values are only approximately 1.5 times higher for MAP+RC as compared with 2D FBP and 2D OSEM.

A similar trend is observed for the transverse line profile of a vertebra of the rat injected with Cu-DO3P for the three Cu isotopes from each reconstruction method (Fig. 6). Because the Cu-DO3P agent accumulates in bone, there is no uptake in the vertebral foramen. The images reconstructed with MAP+RC give the best peak to valley ratio and show low activity in the vertebral foramen. For ^{61}Cu and ^{64}Cu, the activity in the foramen is seen to be almost zero for the MAP+RC reconstructions, whereas for ^{60}Cu, the valley is approximately 50% of the activity in the vertebra.

4. Discussion

The line source phantom showed that at 20 iterations, the spatial resolution of MAP images has reached its minimum value and that slightly more iterations are needed to achieve a similar resolution with a long-range positron emitter such as ^{60}Cu. This last result was also confirmed by the Derenzo phantom, which showed better rod separation with a higher number of iterations when imaging with ^{60}Cu. The absolute value of the obtained resolution with MAP+RC (which is practically identical for all three isotopes) was obtained from a line source surrounded by a cold background. Such conditions can be reproduced when using a tracer with high specific uptake such as a bone-seeking agent. In situations where the uptake is not specific, the spatial resolution with MAP may vary. Anyhow, these initial resolution measurements with the

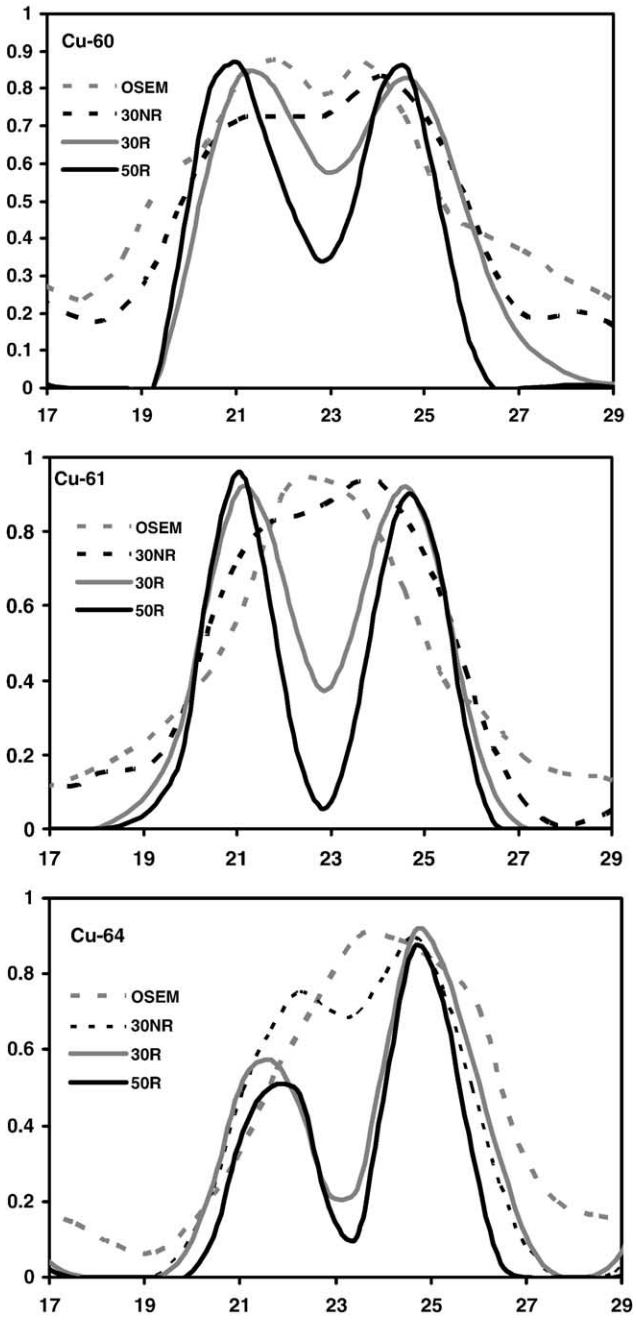

Fig. 6. The line profiles across a vertebra of the rat injected with Cu-DO3P from images reconstructed with 2D OSEM, MAP (30 iterations) and MAP+RC (30 and 50 iterations).

line source indicated a first level of improved resolution due to the accurate system modeling and additional improved performance due to the range correction.

Similarly, the image quality evaluated from the Derenzo phantom images revealed comparable characteristics for the three isotopes. Phantoms of this sort are not typical of contrast in living subjects but instead depict an infinite contrast situation. Phantoms are thus an ideal case for which we would expect the resolution recovery algorithm to work best. We observed rod shapes with distortions (elongated), which are attributable mainly to the imperfection of the system model (i.e., the geometry and sinogram blur kernels). By accurately modeling the block structure of the PET scanner in geometry and blur kernels, the distortions can be reduced significantly. In this study, we did not model the block structure in geometry matrix because it appears that there are less additional advantages. Ignoring the block structure in geometry matrix will cause some distortions, and in calculating the blur kernels, we made several simplifications that may have introduced errors in the resulting kernels and thus caused distortions. For one assumption, we assumed that the energy resolution is perfect and we ignored the difference between direct-plane sinograms and oblique sinograms. We are presently investigating the effect of improved blur kernels on image quality. The ring artifacts most apparent in ^{60}Cu-Derenzo are due to a mismatch of normalization. We have developed a statistical normalization procedure for MAP reconstruction, but its implementation on the microPET-R4 scanner is not finished yet. For these reconstructions, we used the normalization protocol that assumes a system model different from MAP as proposed by the manufacturer.

However, animal imaging experiments using two very different tracers with different specific biodistributions also revealed substantial improvement in image quality from the improved resolution using MAP+RC. In Reference [8], it was shown that the images have less noise with MAP than with FBP at a comparable spatial resolution. It is thus likely that the same conclusion will be valid when the range correction is applied. The line profiles through the kidneys (with PTSM) and vertebrae (with DO3P) revealed the presence of substantial activity in the medulla or foramen with a long-range positron emitter of ^{60}Cu that was not perceptible with ^{64}Cu. High-energy positrons emitted within the cortex can propagate in tissue and annihilate in the medulla or foramen, thus mimicking tracer accumulation. In the absence of adequate range calculation, this activity can be inaccurately associated with radioactivity in the wrong compartment, either in urine or in the spinal cord in these cases. The use of MAP with range correction was clearly beneficial as it yielded a similar distribution of the activity for all three isotopes.

Alternative techniques have been proposed to correct for the positron range, including attempts to recover spatial resolution using Fourier deconvolution [28,29]. However, for a given spatial resolution, this technique can significantly increase the statistical noise. Although a certain degree of noise amplification is inevitable in resolution recovery, the incorporation of positron range correction within the Bayesian framework of MAP allows control of noise amplification versus resolution recovery through a parameter that determines the degree of influence of the prior distribution or smoothing function. The MAP algorithm, used for small-animal imaging without positron range correction, has been shown to produce both improved resolution overall and improved resolution versus noise

properties in phantom and animal experiments [8]. Our experiments confirmed the improved resolution achievable with this approach and showed that a positron range correction is possible and can potentially lead to increased quantitative accuracy in the measurement of the activity in small organs or structures, especially when a long-range positron emitter is used.

The observation that noise increases with the gain in resolution suggests that a smaller value of β and/or a high number of iterations might be appropriate for studies with a high specific uptake in small tumors or organs whereas a larger value of β and/or less iteration might be preferable for uptake in larger organs showing uniform uptake. Quantitation accuracy will thus depend on the choice of these parameters and a careful calibration procedure will need to be adopted. Further studies with phantoms of various sizes (and with different levels of contrast) are required to establish the performance characteristic of the MAP algorithm with the range correction in terms of quantitative accuracy and noise behavior.

In a homogeneous medium, the distribution of annihilation points for positrons emitted from a point source will be isotropic and spatially invariant. Consequently, the range effect can be modeled as a shift-invariant convolution kernel applied to the source distribution prior to forward projection [28,29], as was used in these reconstructions. Inhomogeneous media require anisotropic and spatially variant convolutional kernels that can be determined using either deterministic or Monte Carlo calculations [9]. Although these latter kernels better represent range effects in vivo, accurate implementation in acceptable reconstruction times is difficult, and we have observed that a homogeneous model is sufficient to achieve a reasonable degree of resolution recovery in small-animal studies.

Further development of the algorithm is also underway, consequently as well as an inhomogeneous model where the algorithm can take advantage of a coregistered microCT to determine the body boundary and the internal organ density (i.e., soft tissue, bone, lungs) and where a spatially variant positron range kernel could be used. Alternatively, in a hybrid "truncated homogeneous" model, it can be assumed that positrons that leave the body are not detected, which are modeled approximately by simply truncating the shift-invariant isotropic blur kernels at the boundary of the animal. The cost for the spatial resolution gain is paid in reconstruction time. Although the MAP with positron range algorithm takes the same time as the regular version of MAP, image reconstruction times of 20–30 min are required for the microPET-R4 data (essentially one iteration per minute) using a dual CPU Pentium PC. Such reconstruction times are manageable for static studies but can become prohibitively long for dynamic studies. A message parsing interface-based cluster code is being developed, and initial results indicate that a four-node Opteron PC cluster can reconstruct a microPET-R4 single-frame data set in approximately 4 min. In addition, improvements in the inverse FORE projector that can speed up MAP by 4–10 times are being made. Although still preliminary results at this time, a few avenues are possible to speed up MAP and are being investigated to make its routine use practical.

5. Conclusion

When using a long-range positron emitter such as ^{60}Cu for PET, spatial resolution is limited by the positron range, particularly in high-resolution small-animal PET. We have shown that positron range correction is possible using the MAP image reconstruction framework. The positron range model was included in the system model to recover spatial resolution when high-energy positron emitting isotopes were used. Further investigations are needed to establish the quantitative benefit for spatial resolution on recovery coefficients, particularly with respect to the noise level in the images.

Acknowledgments

This work was supported by NCI (R24 CA 086307) and by NIBIB (R01 EB 00363). Small-animal PET imaging was partially supported by an NIH/NCI SAIRP grant (R24 CA 083060), with additional support from the Small-Animal Imaging Core of the Alvin J. Siteman Cancer Center, which is supported by an NCI Cancer Center support grant (P30 CA 091842). R. Leahy and B. Bai were paid consultants to CTI-Concorde Microsystems when this work was performed.

We thank Dr. Yuan-Chuan Tai for the many helpful discussions shared. We also thank John Engelbach, Nicole Fettig, Lori Strong, Margaret M. Morris and Jerrel Rutlin for their technical assistance.

References

[1] Lewis JS, Achilefu S, Garbow JR, Laforest R, Welch MJ. Small animal imaging. Current technology and perspectives for oncological imaging. Eur J Cancer 2002;2173–88.

[2] McCarthy DW, Shefer RE, Klinkowstein RE, et al. Efficient production of high specific activity ^{64}Cu using a biomedical cyclotron. Nucl Med Biol 1997;24:35–43.

[3] McCarthy DW, Bass LA, Cutler PD, Shefer RE, Klinkowstein RE, Herrerro P, et al. High purity production and potential applications of copper-60 and copper-61. Nucl Med Biol 1999;26:351–8.

[4] Laforest R, Rowland DJ, Welch MJ. MicroPET imaging with nonconventional isotopes. IEEE Trans Nucl Sci 2002;49:2119.

[5] Qi J, Leahy RM, Cherry SR, Chatziioannou A, Farquhar TH. High-resolution 3D Bayesian image reconstruction using the microPET small-animal scanner. Phys Med Biol 1998;43:1001–13.

[6] Qi J, Leahy RM, Hsu C, Farquhar TH, Cherry SR. Fully 3D Bayesian image reconstruction for the ECAT EXACT HR+. IEEE Trans Nucl Sci 1998;45:1096–103.

[7] Mumcuoglu EU, Leahy RM, Cherry SR. Bayesian reconstruction of PET images: methodology and performance analysis. Phys Med Biol 1996;41:1777–807.

[8] Chatziioannou A, Qi J, Moore A, et al. Comparison of 3-D maximum a posteriori and filtered backprojection algorithms for high-resolution

animal imaging with microPET. IEEE Trans Med Imaging 2000; 19:507–12.

[9] Bai B, Ruangma A, Laforest R, Tai YC, Leahy RM. Positron range modeling for statistical PET image reconstructionIEEE Trans Nucl Sci-MIC Proc 2003 [Portland, OR].

[10] Anderson CJ, Jones LA, Bass LA, et al. Radiotherapy, toxicity and dosimetry of copper-64-TETA-octreotide in tumor bearings rats. J Nucl Med 1998;39:1944–51.

[11] Fujibayashi Y, Taniuchi H, Yonekura Y, Ohtani H, Konishi J, Yokoyama A. Copper-62-ATSM: a new hypoxia imaging agent with high membrane permeability and low redox potential. J Nucl Med 1997;38:1155–60.

[12] Fujibayashi Y, Matsumoto K, Yonekura Y, Konishi J, Yokoyama A. A new zinc-62/copper-62 generator as copper-62 source for PET radiopharmaceuticals. J Nucl Med 1989;30:1838–42.

[13] Anderson CJ, Dehdashti D, Cutler PD, et al. ^{64}Cu-TETA-octreotide as a PET imaging agent for patients with neuroendocrine tumors. J Nucl Med 2001;42:213–21.

[14] Shelton ME, Green MA, Mathias CJ, Welch MJ, Bergmann SR. Assessment of regional myocardial and renal blood flow with copper-PTSM and positron emission tomography. Circulation 1990; 82:990–7.

[15] Connett JM, Anderson CJ, Guo LW, et al. Radioimmunotherapy with ^{64}Cu-labeled monoclonal antibody: a comparison with ^{67}Cu. Proc Natl Acad Sci 1996;93:6814–8.

[16] Shelton ME, Green MA, Mathias CJ, Welch MJ, Bergmann SR. Kinetics of copper-PTSM is isolated hearts: a novel tracer for measuring blood flow with positron emission tomography. J Nucl Med 1989;30:1843–7.

[17] Lewis MR, Wang M, Axworthy DB, et al. In vivo evaluation of pretargeted ^{64}Cu for tumor imaging and therapy. J Nucl Med 2003; 44:1284–92.

[18] Dehdashti F, Mintun MA, Lewis JS, et al. In vivo assessment of tumor hypoxia in lung cancer with ^{60}Cu-ATSM. Eur J Nucl Med Mol Imaging 2003;30:844–50.

[19] Sun X, Wuest M, Kovacs Z, et al. In vivo behavior of copper-64-labeled tetraazamacrocyclic methanephosphonate ligands. J Biol Inorg Chem 2003;8:217–25.

[20] Young H, Carnochan P, Zweit J, Babich J, Cherry S, Ott RJ. Evaluation of copper(II)-pyruvaldehyde bis(N^4-methylthiosemicarbazone) for tissue blood flow measurement using a trapped tracer model. J Nucl Med 1994;21:336–41.

[21] Fujibayashi Y, Cutler CS, Anderson CJ, et al. Comparative studies of Cu-64-ATSM and C-11-acetate in an acute myocardial infarction model: ex vivo imaging of hypoxia in rats. Nucl Med Biol 1999; 26:117–21.

[22] Knoess C, Siegel S, Smith A, et al. Performance evaluation of the microPET R4 PET scanner for rodents. Eur J Nucl Med 2003;30.

[23] Yavuz M, Fessler JA. Statistical image reconstruction methods for randoms-precorrected PET scans. Med Im Anal 1998;2:369–78.

[24] Bielajew AF, Rogers DWO. PRESTA: the parameter reduced electron-step transport algorithm for electron Monte Carlo transport. Nucl Instr Methods Phys B 1987;18:165–81.

[25] Nelson WR, Hirayama H, Rogers DWO. The EGS4 code system. SLAC report 265 1985.

[26] Monte Carlo transport of electrons and photons. Plenum; 1988. p. 287–306.

[27] Derenzo SE, Budinger TF, Juesman RH, Cahoon JL, Vuletich T. Imaging properties of a positron tomograph with 280 BGO crystals. IEEE Trans Nucl Sci 1981;28:81–9.

[28] Derenzo SE. Mathematical removal of positron range blurring in high resolution tomography. IEEE Trans Nucl Sci 1986;33:565–9.

[29] Haber SF, Derenzo SE, Uber D. Application of mathematical removal of positron range blurring in positron emission tomography. IEEE Trans Nucl Sci 1990;37:1293–9.